Electronic Supplementary Information for

Chiral hybrid manganese (II) chloride single crystals for achieving second harmonic generation and moderate circularly polarized luminescence

Teng Li,[a] Yue Wang,[b] Yanqing Liu,[a] Guokui Liu,[c] Lingqiang Meng,*[d] Yongshen Zheng*[b] and Yangyang Dang*[a]

[a] School of Physics and Physical Engineering, Qufu Normal University, Qufu 273165, P. R. China.

[b] School of Materials Science and Engineering, Smart Sensing Interdisciplinary Science Center, Nankai University, Tianjin 300350, P. R. China.

[c] School of Chemistry and Chemical Engineering, Linyi University, Linyi 276000, P. R. China.

[d] School of Advanced Materials, Peking University Shenzhen Graduate School, Peking University, Shenzhen 518055, P. R. China.

Corresponding Authors: Email: dyy@qfnu.edu.cn; yszheng@nankai.edu.cn；menglingqiang@pku.edu.cn

Experimental Section

Fig. S1. Crystal preparation processing. (a) Colored solutions and (b) Colorless crystals of (*R/S*-2-mpip)$MnCl_4·2H_2O$ and (*rac*-2-mpip)$MnCl_4·2H_2O$.

Fig. S2. TGA diagram of (*R*/*S*-2-mpip)$MnCl_4·2H_2O$ and DSC diagram of (*R*/*S*-2-mpip)$MnCl_4·2H_2O$ and (*rac*-2-mpip)$MnCl_4·2H_2O$.

Fig. S3. XPS spectra for (*R*-2-mpip)$MnCl_4·2H_2O$ single crystals..

Fig. S4. XPS spectra for (*S*-2-mpip)$MnCl_4·2H_2O$ single crystals.

Fig. S5. XPS spectra for (*rac*-2-mpip)$MnCl_4·2H_2O$ single crystals.

Fig. S6. Nonlinear optical properties of (*S*-2-mpip)$MnCl_4·2H_2O$.

Fig. S7. UV-vis spectra and optical band gap of (a)(*R*-2-mpip)$MnCl_4·2H_2O$(heated), (b) (*S*-2-mpip)$MnCl_4·2H_2O$(heated) and (c) (*rac*-2-mpip)$MnCl_4·2H_2O$(heated).

Fig. S8. PLQY of (a)(*R*-2-mpip)$MnCl_4·2H_2O$(heated), (b)(*S*-2-mpip)$MnCl_4·2H_2O$(heated) and (c)(*rac*-2-mpip)$MnCl_4·2H_2O$(heated).

Fig. S9. Comparison of photoluminescence under different UV irradiations at room temperature and after heating to 383K.

Fig. S10. Cyclic luminescent phase transitions are achieved by spraying water, drying, and then reheating to 383K.

Fig. S11. Cyclic luminescent phase transitions are achieved by spraying anhydrous ethanol, drying, and then reheating to 383K.

Table S1. Crystal data of (*R*/*S*-2-mpip)$MnCl_{4}.2H_2O$ and (*rac*-2-mpip)$MnCl_{4}.2H_2O$.

Table S2. The bond valence sum (BVS) for (*R*-2-mpip)$MnCl_4·2H_2O$.

Table S3. The bond valence sum (BVS) for (*S*-2-mpip)$MnCl_4·2H_2O$.

Table S4. The bond valence sum (BVS) for (*rac*-2-mpip)$MnCl_{4}.2H_2O$.

Table S5. Summary of chiral manganese halides in recently published literature.

References

Experimental Section

Powder and Single Crystal X-ray Diffraction Measurements. Powder X-ray diffraction patterns were measured on a *PANalytical XPert Pro MPD* equipment with Cu-K_a radiation in the 2θ range of 10-80°using reasonable step size and step time settings. Single-crystal X-ray diffraction data were collected on a *Bruker* D8 advance diffractometer equipped with a CCD detector (graphite-monochromated Mo-K_a radiation, λ= 0.71073 Å) at 293.15 K. *APEX3* software was used for data integration and cell refinements. The crystal was kept at 293.15 K during data collection. Using *Olex2*,[1] the structure was solved with the *Olex2*.solve[2] structure solution program using Charge Flipping and refined with the *XL*[3] refinement package using *Least Squares minimization.*

X-ray Photoelectron Spectroscopy (XPS) Measurements. Polycrystalline samples were extracted using a sample transporter that protects against air exposure. The sample transporter is connected to the ultra-high vacuum chamber and then transferred to the XPS systems for characterizations. Pass energy values are 160 eV for XPS wide scan, 10 eV for high resolution scan. All the data analysis about XPS was performed using the *XPS Peaks Fit software*. All the elements were fitted with the 70% Gaussian and 30% Lorentzian peak shapes after applying background subtractions with *Shirley* function.

Theoretical Calculations. The Vienna ab initio simulation package (VASP) was employed to perform structural optimization using the conjugate gradient method.[4] The Perdew, Burke, and Ernzerhof exchange-correlation functional within GGA was used.[5-8] In the self-consistent process, the convergence of energy between the two electronic steps was set to 10-5 eV. Ionic relaxation was ceased once the maximum force fell below 0.02 eV/Å. During the optimization process, all atoms in the models including the cell shape and volume were allowed to fully relax. For the reciprocal space sampling, the Monkhorst-Pack grids of (*R* -2-mpip)$MnCl_4\cdot 2H_2O$, (*S*-2-mpip)$MnCl_4\cdot 2H_2O$, (*rac*-2-mpip)$MnCl_4\cdot 2H_2O$ were set to 4×5×3, 4×5×3, 3×5×2 respectively. Finally, a plane-wave expansion of electronic wave functions was conducted with an energy cutoff of 450 eV. For all systems, the effect of spin polarization is considered.

Optical Measurements. The UV-vis diffuse spectra were measured using a UV-vis-NIR absorption spectrophotometer (*PerkinElmer, Lambda 1050*). A $BaSO_4$ plate was used as the standard (100% reflectance) on which the finely ground sample from the crystal was coated. The absorption spectrum was calculated from the reflectance spectrum using the Kubelka-Munk function,[9]

$$F(R)=\alpha/S = (1-R)^2/(2R)$$ (**Equation 1**)

where α is the absorption coefficient, S is the scattering coefficient, and R is the reflectance.

The (*R*/*S*-2-mpip)$MnCl_4\cdot 2H_2O$ and (*rac*-2-mpip)$MnCl_4\cdot 2H_2O$ crystals were first grinded into powders and then heated on a heating stage. According to the combined analysis of TGA and DSC spectra, both (*R*/*S*-2-mpip)$MnCl_4\cdot 2H_2O$ and (*rac*-2-mpip)$MnCl_4\cdot 2H_2O$ began to lose water when heated to 371K. A phase transition peak appeared around 381K for all samples, and complete dehydration occurred until heated to approximately 398K. Afterward, the powders were cooled to room temperature, and the PL spectra of (*R*/*S*-2-mpip)$MnCl_4\cdot 2H_2O$ (heated) and (*rac*-2-mpip)$MnCl_4\cdot 2H_2O$ (heated) were measured.

Fluorescence spectra of (*R*/*S*-2-mpip)$MnCl_4\cdot 2H_2O$ and (*rac*-2-mpip)$MnCl_4\cdot 2H_2O$ based single-crystalline samples were measured on an Edinburg FLS-1000 fluorescence spectrometer using a xenon lamp as the excitation source. The absolute fluorescence quantum yield (PLQY) was measured by using an absolute PL quantum yield spectrometer (Edinburg FLS-1000 fluorescence spectrometer) with a calibrated integrating sphere and fluorescence lifetime measurements were recorded on the same spectrometer using time-correlated single photon counting systems based on polytetrafluoroethylene (PTFE). The sample is placed in a PTFE-coated cuvette, the sample is excited using a pulsed light source with a high repetition rate, and the temporal distribution of fluorescent photons is recorded by the TC-SPC system. The combination of PTFE material and TC-SPC technology not only reduces the loss of photons, but also the low-fluorescence property of PTFE reduces the background signal and improves the signal-to-noise ratio, and its chemical stability and corrosion resistance prolongs the service life of the equipment.

We tested the CD data of (*R/S*-2-mpip)$MnCl_4\cdot 2H_2O$ using the KBr disk method. Firstly, a mixture of the chiral compound (*R/S*-2-mpip)$MnCl_4\cdot 2H_2O$(heated) and KBr was prepared. The mixture was thoroughly ground in a mortar and pestle. Secondly, the resulting mixture was compressed under a pressure of 20 MPa to form thin and transparent pellet.[10] The key to obtaining accurate CD spectra lies in preparing samples in an optically isotropic state. The CD curves measured on both sides of the KBr pellet samples and at different angles were similar, further confirming the isotropic nature of the KBr pellet samples. And CD data was tested on Circular Dicroroism Spectrometer, model: Chirascan V100, Applied Photophysics (Surry, UK).

Circularly polarized luminescence (CPL) emission spectra were obtained using a JASCO CPL-300 instrument.[11] The chiral (*R*/*S*-2-mpip)$MnCl_4 \cdot 2H_2O$ single crystal sample film was placed in the sample bath of the instrument. The crystal was placed in the optical path so that the optical path is perpendicular to the smooth crystal plane as much as possible, the excitation wavelength was set to 365 nm, and the collection wavelength around 675 nm, but the actual wavelength may be slightly different. The scanning range was from 500 nm to 750 nm. The luminescence dissymmetry factor (g_{lum}) was calculated,

$$g_{lum}=\Delta I/I=2(I_L-I_R)/(I_L+I_R) \quad \textbf{(Equation 2)}$$

where I_L and I_R, are the luminous intensity of LCP light and RCP light, respectively.

First, polarization anisotropy affects the intensity and directionality of the CPL signal causing the polarization state to change, thus affecting the symmetry and intensity of the CPL signal. And light is decomposed into two light components with different polarization directions (o light and e light). Birefringence not only causes a phase delay between light components with different polarization directions; it also changes the polarization state of the incident light, which in turn affects the circular polarization of the CPL signal. Second, impurities in the sample introduce additional luminescent signals that interfere with the CPL properties of the target molecule, leading to a decrease in signal purity. The microstructure (e.g., grain size) and macrostructure (e.g., sample height deviation) of the sample can affect the isotropy and anisotropy of the CPL signal. Excessive sample concentration or inhomogeneous distribution may lead to nonlinear variations in the signal or localized self-absorption phenomena, which may reduce the purity of the CPL signal. Samples may undergo chemical reactions or physical changes during the measurement process, resulting in signal drift or distortion, which affects the purity of the CPL signal.

NLO Measurements. The single crystal NLO measurements were examined with a home-built scanning microscope with a femtosecond laser system (Mai Tai HP, < 100 fs, 80 MHz, spot diameter ~20 μm, wavelength tunable from 690 to 1040 nm (800 to 1040 nm) for both (*R*-2-mpip)$MnCl_4\cdot 2H_2O$ and (*S*-2-mpip)$MnCl_4\cdot 2H_2O$ in the reflection geometry, with the incidence and detection angles both at 45°. The measured SHG signal is reflected from the front surface of the sample.

Thermogravimetric analysis measurements. Thermogravimetric analysis (TGA) was carried out using a TGA/DSC1/1600HT analyzer (METTLER TOLEDO Instruments). All the powder samples were placed in an Al_2O_3 crucible, and heated at a rate of 10°C min^{-1} from room temperature to 600°C under flowing N_2 gas, respectively.

Differential Scan Calorimetry (DSC). The powder samples were placed in Al crucible, and heated at a rate of 10 °C min^{-1} from 293K to 398K under flowing N_2 gas, respectively. Differential Scan calorimetry (DSC) measurements were performed on *NETZSCH* Instruments (DSC 214 Polyma).

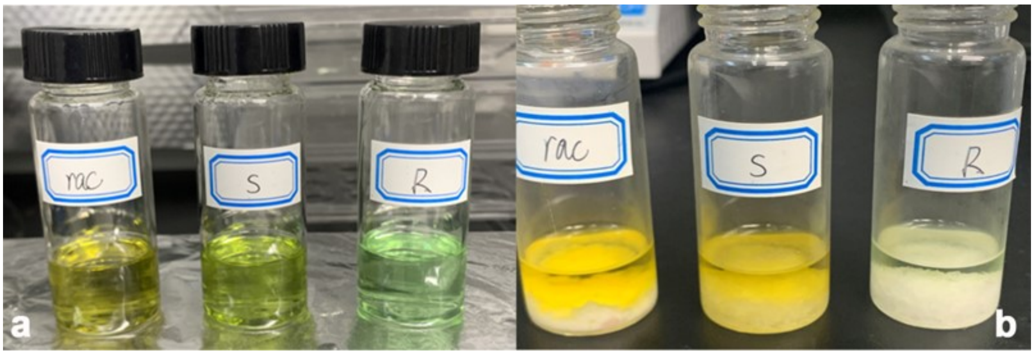

Fig. S1. Crystal preparation processing. (a) Colored solutions and (b) Colorless crystals of (*R/S*-2-mpip)$MnCl_4\cdot 2H_2O$ and (*rac*-2-mpip)$MnCl_4\cdot 2H_2O$.

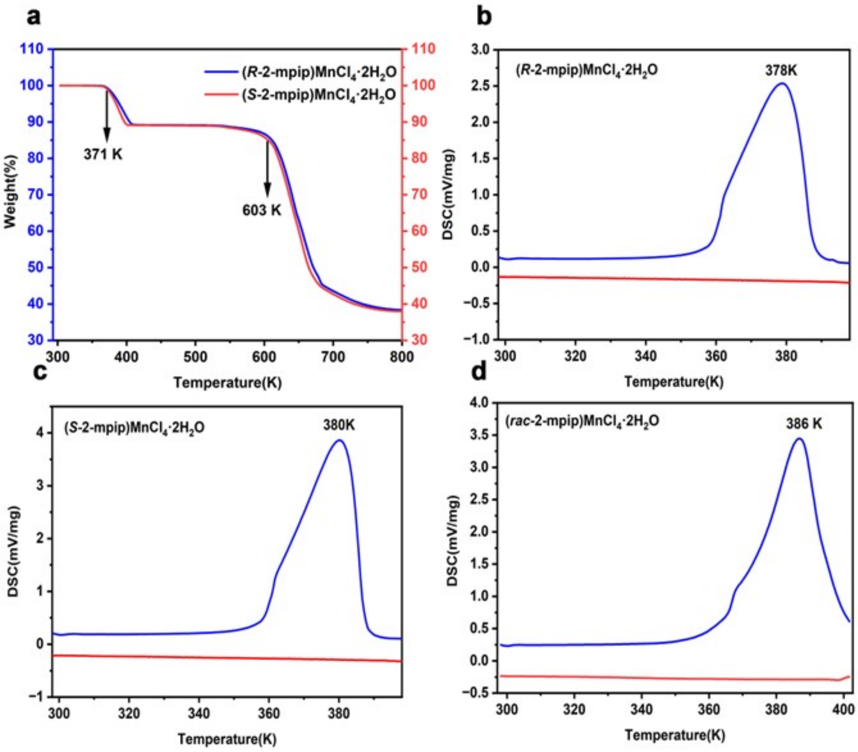

Fig. S2. TGA diagram of (*R*/*S*-2-mpip)$MnCl_4·2H_2O$ (a) and DSC diagram of (*R*/*S*-2-mpip)$MnCl_4·2H_2O$ (b, c) and (*rac*-2-mpip)$MnCl_4·2H_2O$ (d).

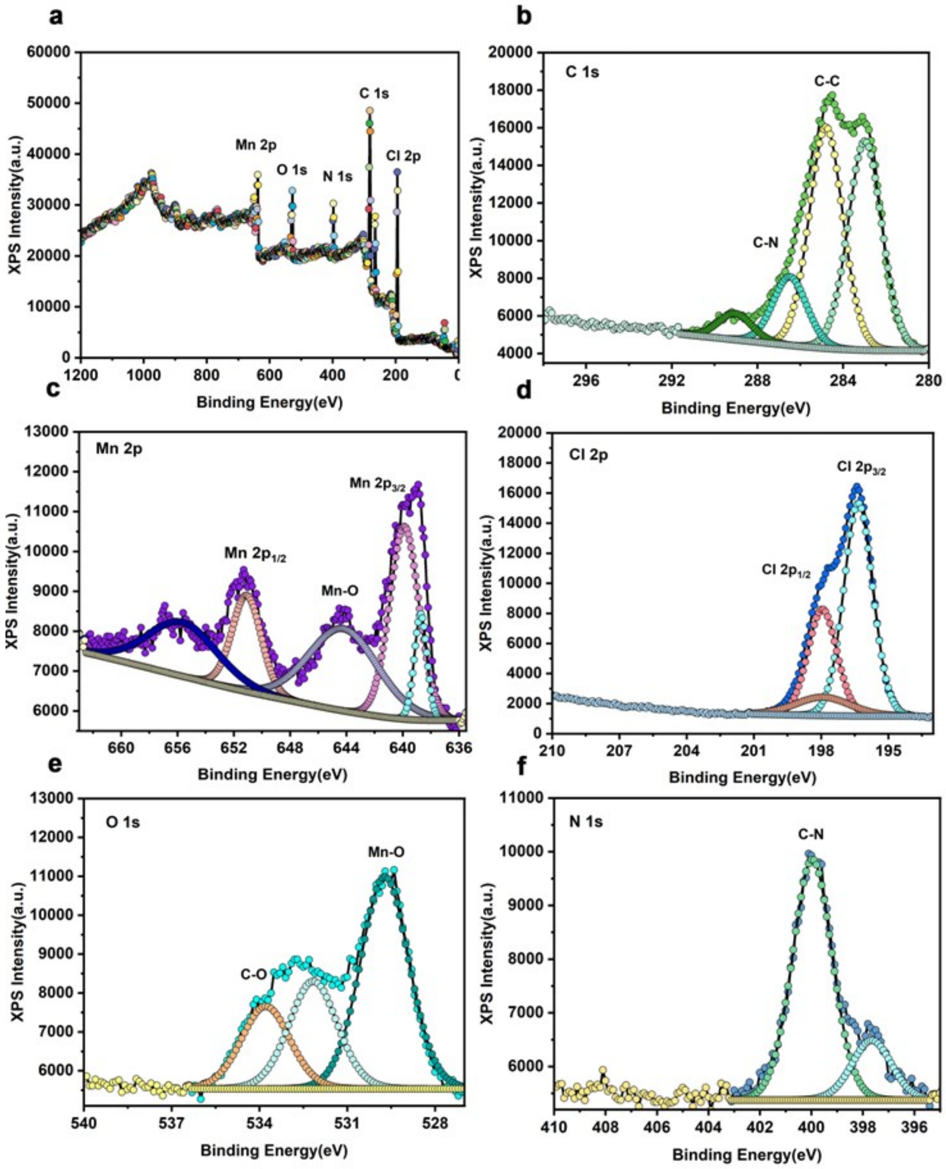

Fig. S3. XPS spectra for (R-2-mpip)$MnCl_4 \cdot 2H_2O$ single crystals. Core level XPS spectra for (a) wide scan of (R-2-mpip)$MnCl_4 \cdot 2H_2O$ single crystals, (b) C 1s, (c) Mn 2p, (d) Cl 2p, (e) O 1s (f) N 1s, fitted with peaks having an 70% Gaussian and 30% Lorentzian peak shape after applying background subtraction with Shirley function.

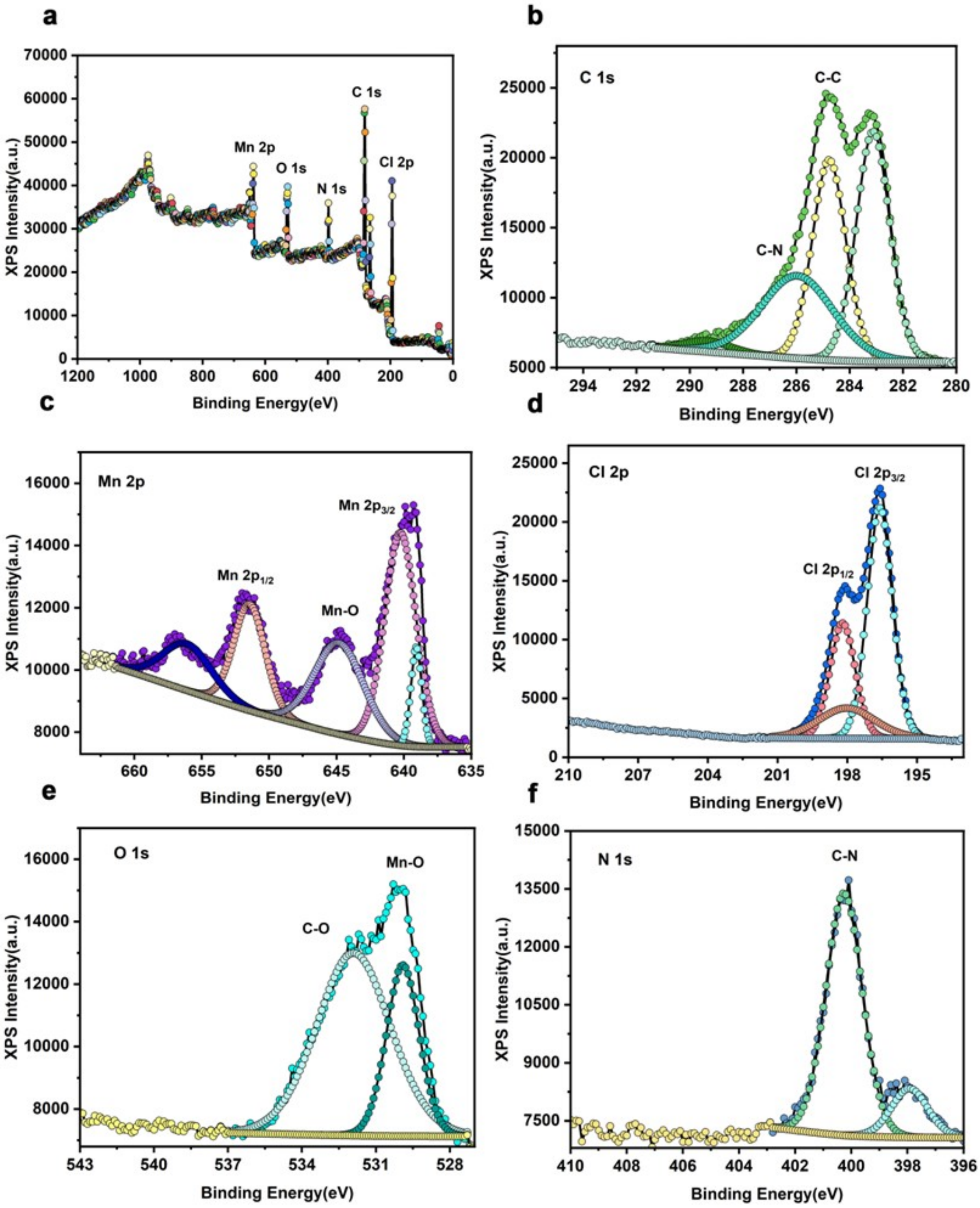

Fig. S4. XPS spectra for (*S*-2-mpip)$\mathrm{MnCl_4{\cdot}2H_2O}$ single crystals. Core level XPS spectra for (a) wide scan of (*S*-2-mpip)$\mathrm{MnCl_4{\cdot}2H_2O}$ single crystals, (b) C 1s, (c) Mn 2p, (d) Cl 2p, (e) O 1s (f) N 1s ,fitted with peaks having an 70% Gaussian and 30% Lorentzian peak shape after applying background subtraction with Shirley function.

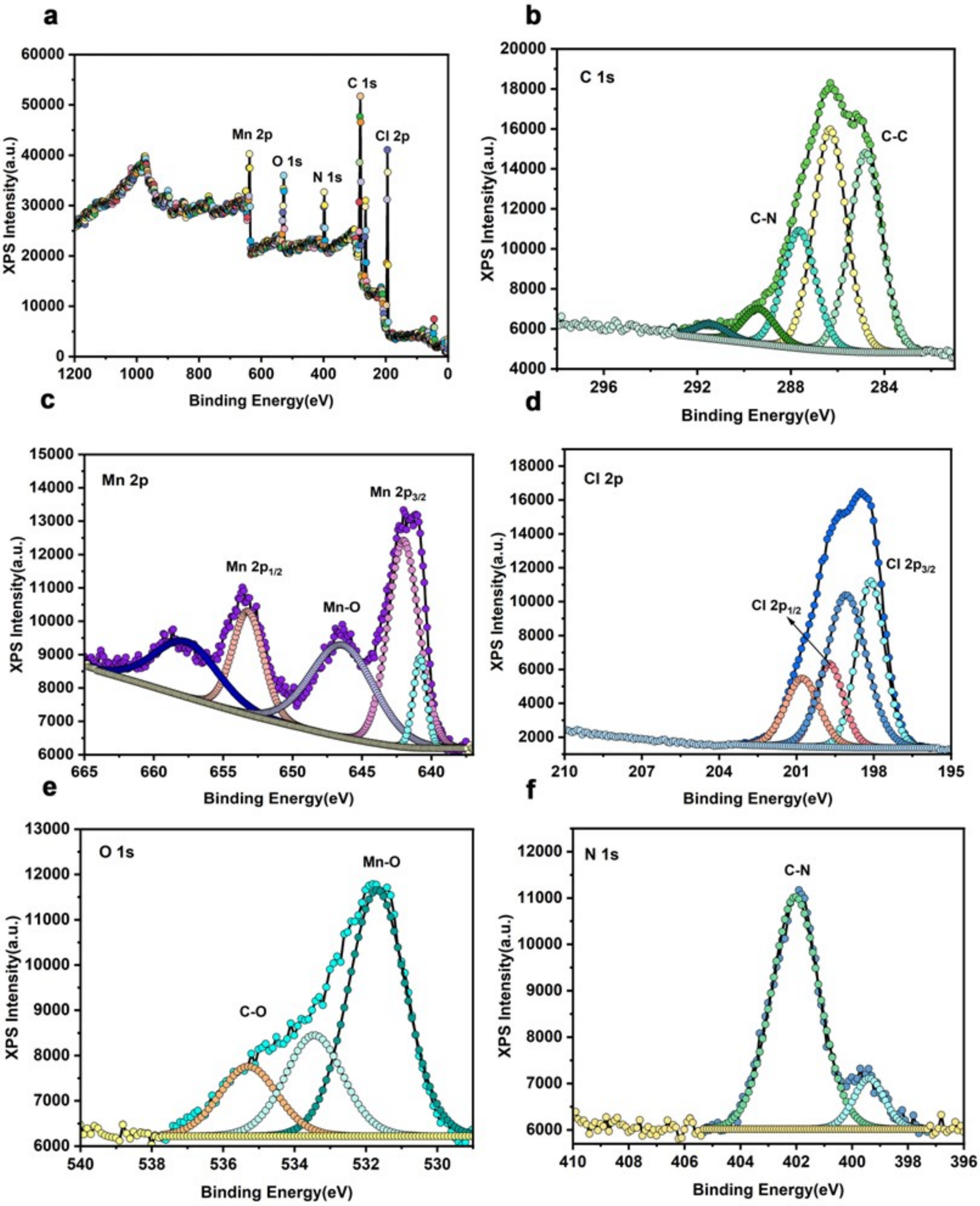

Fig. S5. XPS spectra for (*rac*-2-mpip)MnCl$_4$·2H$_2$O single crystals. Core level XPS spectra for (a) wide scan of (*rac*-2-mpip)MnCl$_4$·2H$_2$O single crystals, (b) C 1s, (c) Mn 2p, (d) Cl 2p, (e) O 1s (f) N 1s, fitted with peaks having an 70% Gaussian and 30% Lorentzian peak shape after applying background subtraction with Shirley function.

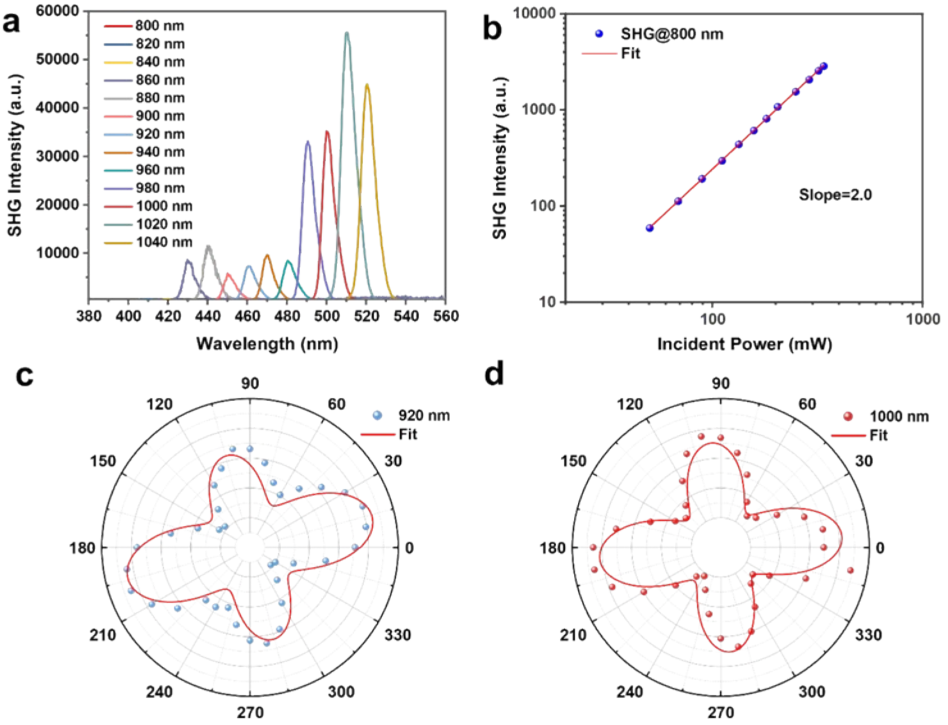

Fig. S6. Nonlinear optical properties of (S-2-mpip)$MnCl_4 \cdot 2H_2O$. (a) Wavelength-dependent SHG spectra of (S-2-mpip)$MnCl_4 \cdot 2H_2O$ from 800 to 1040 nm. Incident power: 50 mW; exposure time: 1 s. (b) Logarithmic curve of the SHG intensity versus incident power of (S-2-mpip)$MnCl_4 \cdot 2H_2O$ at 800 nm. The red line is the linear fitting of data points with a slope of 2.0. The SHG intensity of (S-2-mpip)$MnCl_4 \cdot 2H_2O$ at various polarized angles of (c) 920 nm and (d) 1000 nm lasers. The red line is the nonlinear fitting of data points.

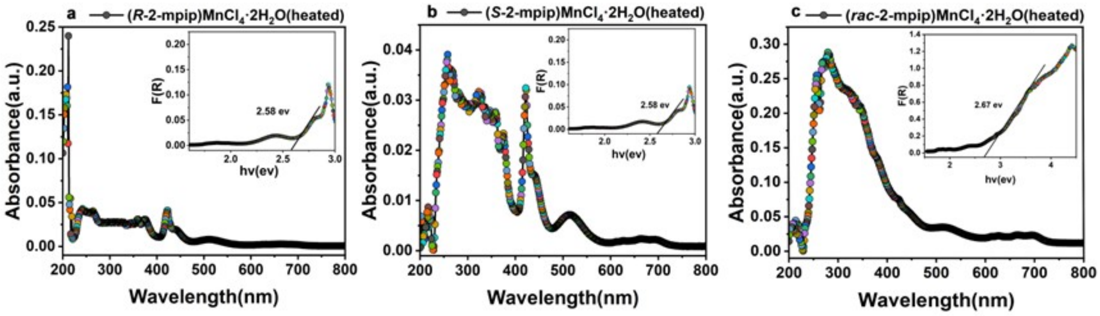

Fig. S7. UV-vis spectra and optical band gap of (a)(R-2-mpip)$MnCl_4 \cdot 2H_2O$(heated), (b) (S-2-mpip)$MnCl_4 \cdot 2H_2O$(heated) and (c) (rac-2-mpip)$MnCl_4 \cdot 2H_2O$(heated).

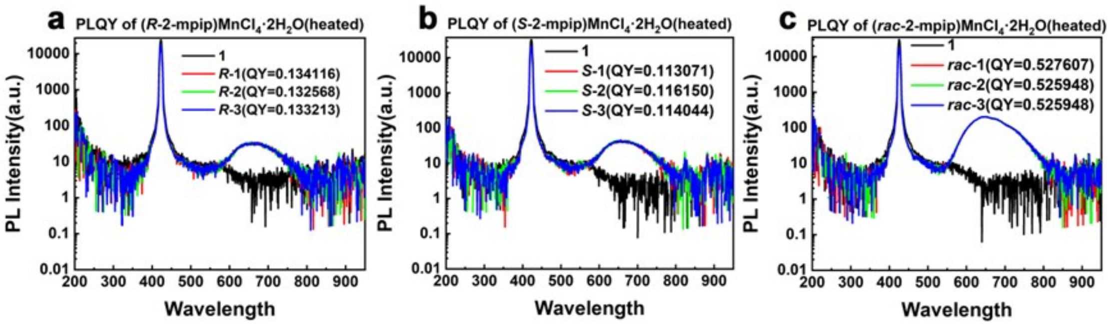

Fig. S8. PLQY of (a)(*R*-2-mpip)MnCl$_4$·2H$_2$O(heated), (b)(*S*-2-mpip)MnCl$_4$·2H$_2$O(heated) and (c)(*rac*-2-mpip)MnCl$_4$·2H$_2$O(heated).

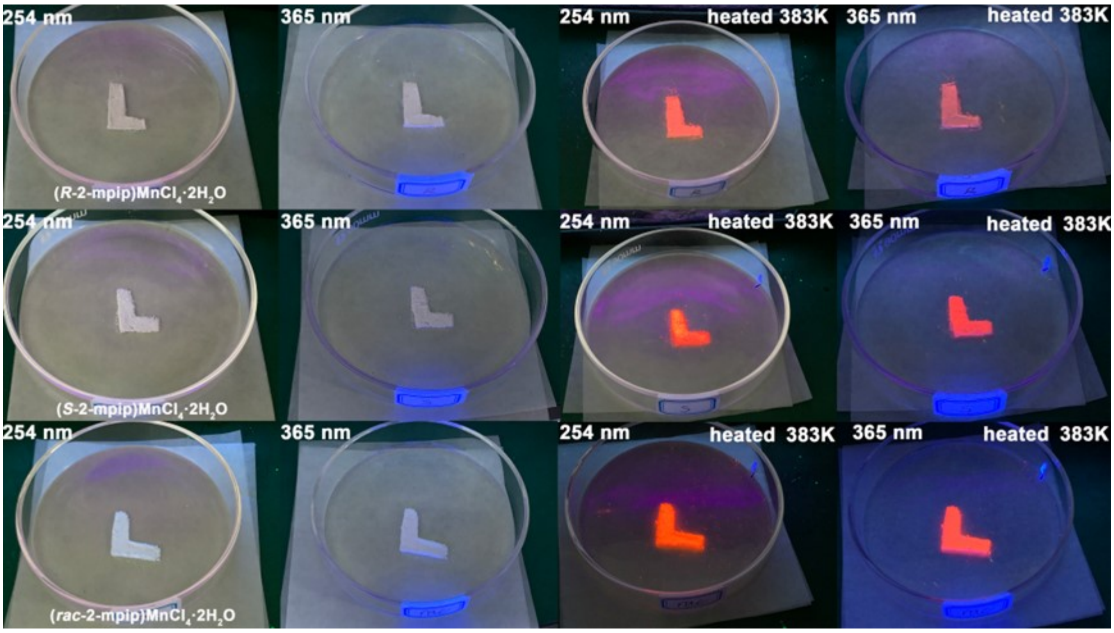

Fig. S9. Comparison of photoluminescence under different UV irradiations at room temperature and after heating to 383K.

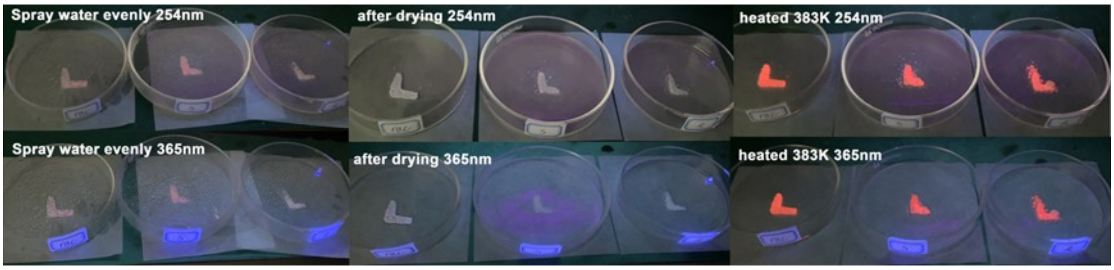

Fig. S10. Cyclic luminescent phase transitions are achieved by spraying water, drying, and then reheating to 383K.

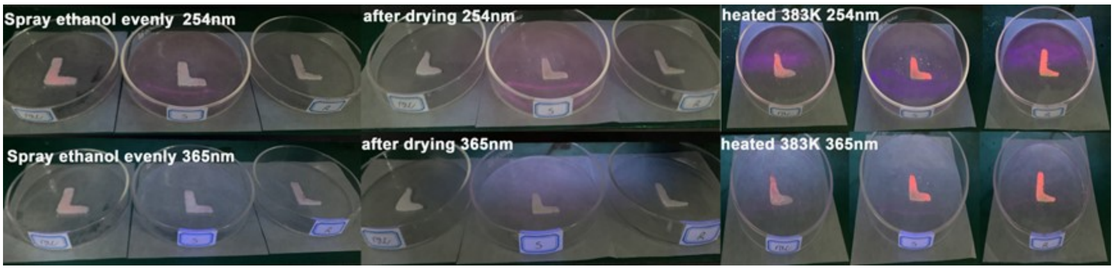

Fig. S11. Cyclic luminescent phase transitions are achieved by spraying anhydrous ethanol, drying, and then reheating to 383K

Table S1. Crystal data of (*R*/*S*-2-mpip)$MnCl_4\cdot 2H_2O$ and (*rac*-2-mpip)$MnCl_4\cdot 2H_2O$.

Name	(*R*-2-mpip)$MnCl_4\cdot 2H_2O$	(*S*-2-mpip)$MnCl_4\cdot 2H_2O$	(*rac*-2-mpip)$MnCl_4\cdot 2H_2O$
Empirical formula	$C_5H_{18}Cl_4MnN_2O_2$	$C_5H_{18}Cl_4MnN_2O_2$	$C_5H_{18}Cl_4MnN_2O_2$
weight/g·mol^{-1}	334.95	334.95	334.95
Temperature/K	293.15K	293.15K	293.15K
Wavelength/Å		0.71073	
Crystal color		Colourless	
Crystal system	Monoclinic	Monoclinic	Monoclinic
Space group	$P2_1$ (no.4)	$P2_1$ (no.4)	$P2_{1/c}$ (no.14)
a/Å	8.6660(5)	8.6614(19)	12.0890(8)
b/Å	6.4956(4)	6.4962(13)	6.4455(4)
c/Å	12.0646(7)	12.065(3)	17.3538(12)
α/°	90	90	90
β/°	101.666(2)	101.664(7)	102.238(2)
γ/°	90	90	90
Volume/Å^{-3}	665.10(7)	664.8(2)	1321.47(15)
Crystal size (mm^3)	0.12 × 0.08 × 0.05	0.15 × 0.12 × 0.1	0.15 × 0.12 × 0.1
Z	2	2	4
Density/g·cm^{-3}	1.673	1.673	1.684
μ(mm^{-1})	1.776	1.776	1.787
F (000)	342.0	342.0	684.0
GOF on F^2	1.030	1.051	1.059
Absolute Flack Factor	0.020(9)	0.011(8)	--
Absorption correction		Semi-empirical from equivalents	
Refinement method		Full-matrix least-squares on F^2	
Data / restraints / parameters	3667/1/131	3258/1/131	3259/1/133
R_1, wR_2 [$I > 2\sigma$ (I)]	0.0226, 0.0507	0.0214, 0.0496	0.0278, 0.0553
R_2, wR_2 (all data)	0.0255, 0.0518	0.0240, 0.0505	0.0394, 0.0591
Min/Max Δρ /eÅ^{-3}	-0.34/ 0.29	-0.30/ 0.25	-0.35/ 0.37
CCDC	**2418218**	**2418219**	**2418220**

Table S2. The bond valence sum (BVS) for (*R*-2-mpip)$MnCl_4\cdot 2H_2O$.

	R_0	**B**	**Bond Valence S_{ij}**	**Bond length r_{ij} /Å**
Mn01			2.000264	
Cl02	2.133	0.37	0.284499	2.5981
Cl03	2.133	0.37	0.352405	2.5189
Cl04	2.133	0.37	0.325048	2.5488
Cl05	2.133	0.37	0.352787	2.5185
O06	1.79	0.37	0.347487	2.1811
O07	1.79	0.37	0.338039	2.1913

Table S3. The bond valence sum (BVS) for (*S*-2-mpip)$MnCl_4\cdot 2H_2O$.

	R_0	**B**	**Bond Valence S_{ij}**	**Bond length r_{ij} /Å**
Mn01			2.002413	
Cl02	2.133	0.37	0.284345	2.5983
Cl03	2.133	0.37	0.324433	2.5495
Cl04	2.133	0.37	0.354315	2.5169
Cl05	2.133	0.37	0.353837	2.5174
O06	1.79	0.37	0.348993	2.1795
O07	1.79	0.37	0.336489	2.193

Table S4. The bond valence sum (BVS) for (*rac*-2-mpip)$MnCl_4 \cdot 2H_2O$.

	R_0	**B**	**Bond Valence S_{ij}**	**Bond length r_{ij} /Å**
Mn01			2.038159	
Cl02	2.133	0.37	0.281211	2.6024
Cl03	2.133	0.37	0.346456	2.5252
Cl04	2.133	0.37	0.350127	2.5213
Cl05	2.133	0.37	0.353264	2.518
Cl06	1.79	0.37	0.353837	2.1744
Cl07	1.79	0.37	0.353264	2.175

Table S5. Summary of chiral manganese halides in recently published literature.

Chiral hybridized metal halides	**Emission peaks**	**PLQYs**	**g_{lum}**	**Ref.**
(*R/S*-2-mpip)$MnCl_4 \cdot 2H_2O$ and (*rac*-2-mpip)$MnCl_4 \cdot 2H_2O$	650nm	＞10%	1.2×10^{-3}	This work
R-, *S* and *rac*-(2-methylpiperazine) $MnBr_3$	530nm	12%	1.12×10^{-2}	*J. Mater. Chem. C*， 2025,13, 2190-2197.
(*R*)- and (*S*)-3-(fluoropyrrolidinium)$MnBr_3$	650nm	28.13 and 32.46%	$\pm6.1\times10^{-3}$	*J. Am. Chem. Soc.* 2020, 142(10), 4756-4761.
(*R/S*-1-PPA)$_2MnBr_4$	530nm	9.35 and 13.24%	-1×10^{-2} and 8×10^{-3}	*J. Alloys Compd.* 2022, 910, 164892.
(*R/S*-3-quinuclidinol)$MnBr_3$ (*R/S*-1)	620nm	50.2% of (R-1)	2.3×10^{-2} of (R-1) -2.27×10^{-2} of (S-1)	*Angew. Chem. Int. Ed.* 2022, 61, e202205906.
(D)- and (L)-(tert-butylprolinate)$MnCl_3$	646nm	67.1 % and 57.2 %	6.1×10^{-3} and -6.3×10^{-3}	*Chem. Eur. J.* 2022, 28, e202201
(*R/S*-3-aminopyrrolidine dihydrochloride)$_6$(Mn_3Cl_{12})(Cl)$_6$ **(*R/S*-1)** (*R/S*-1,2-diaminopropane dihydro-chloride)$_3$(Mn_3Cl_{12})**(*R/S*-2)**.	650nm	85% of (*R/S*-2)	7.1×10^{-3} of (R/S-1), $2\times10^{-3}$of (R/S-2)	*J. Mater. Chem. C,* 2023, 11, 3206-3212.
R/S-[MBA-Me_3]$MnBr_4$	519nm	≈1	4.5×10^{-3}	*Adv. Optical*

Mater. 2023, 11, 2202811

References

(1) O. V. Dolomanov, L. J. Bourhis, R. J. Gildea, J. Howard, H. Puschmann, *J. Appl. Crystallogr.,* 2009, **42**, 339-341.

(2) L. J. Bourhis, O. V. Dolomanov, R. J. Gildea, J. Howard, H. Puschmann, *Acta Crystallogr A Found Adv.,* 2015, **71**, 59-75.

(3) G. M. Sheldrick, *Acta Crystallogr A.,* 2008, **64**, 112-122.

(4) G. Kresse, J. Furthmüller, *Comp. Mater. Sci.,* 1996, **6**, 15-50.

(5) G. Kresse, J. Furthmüller, *Phys. Rev. B.,* 1996, **54**, 11169-11186.

(6) J. P. Perdew, K. Burke, M. Ernzerhof, *Phys. Rev. Lett.,* 1996, **77,** 3865-3868.

(7) J. P. Perdew, K. Burke, M. Ernzerhof, *Phys. Rev. Lett.* 1996, **78**, 1396-1396.

(8) H. J. Monkhorst, J. D. Pack, *Phys. Rev. B.,* 1976, **13**, 5188-5192.

(9) W. Wendlandt and H. G. Hecht, *Wiley Interscience. New York.*, 1966.

(10) X. B. Han, W. Wang, M. L. Jin, C. Q. Jing, B. D. Liang, C. Y. Chai, R. G. Xiong and W. Zhang, *Anal. Chem.*, 2023, **95**, 16201−16209.

(11) Y. Kondo, S. Suzuki, M. Watanabe, A. Kaneta, P. Albertini and K. Nagamori, *Front. Chem.*, 2020, **8**, 0057.